Wear 523 (2023) 204731

Contents lists available at ScienceDirect

Wear

journal homepage: www.elsevier.com/locate/wear

Effects of deposition temperature on the wear behavior and material properties of plasma enhanced atomic layer deposition (PEALD) titanium vanadium nitride thin films

Kylie E. Van Meter [a,b], Md Istiaque Chowdhury [c], Mark J. Sowa [d], Alexander C. Kozen [e], Tomas Grejtak [a,b,f], Tomas F. Babuska [a,b,f], Nicholas C. Strandwitz [c], Brandon A. Krick [a,b,f,*]

[a] Department of Mechanical Engineering, Florida A&M University, Florida State University College of Engineering, Tallahassee, FL, 32310-5754, USA
[b] Aero-propulsion, Mechatronics, and Energy Center, Florida A&M University, Florida State University College of Engineering, Tallahassee, FL, 32310, USA
[c] Department of Materials Science and Engineering, Lehigh University, Bethlehem, PA, 18015, USA
[d] Veeco ALD, Waltham, MA, 02453, USA
[e] Department of Materials Science & Engineering, University of Maryland, College Park, MD, 20740, USA
[f] Department of Mechanical Engineering and Mechanics, Lehigh University, Bethlehem, PA, 18015, USA

ARTICLE INFO

Handling Editor: Dr. M Dienwiebel

Keywords:
Ultralow wear nitrides
PEALD nitrides
Depostition temperature
Titanium nitride
Vanadium nitride

ABSTRACT

This work investigates the effects of deposition temperature on the wear behavior and material properties of recently developed plasma enhanced atomic layer deposited (PEALD) TiVN films. ~50–100 nm thick $Ti_xV_{1-x}N$ (x ~ 0.5, hereto referred to as TiVN) films were deposited using PEALD on Si substrates with thermal oxide at a range of deposition temperatures (150 °C, 200 °C, 250 °C, 300 °C, 350 °C). Wear testing was performed on each film using a linearly reciprocating tribometer in a controlled humidity environment. Wear rates of the TiVN films varied with deposition temperature, with the 250 °C sample achieving ultralow wear(5.4×10^{-7} mm^3/Nm), while the 150 °C sample wore through the film completely in early sliding cycles. Along with their low wear properties, these PEALD TiVN films were found to have low electrical resistivity when deposited above 150 °C. Film density and crystallite size increased with increasing deposition temperature up to 250 °C, where these properties plateaued. High compressive residual stresses were measured, ranging from 2.7 to 7.7 GPa. XRD Bragg peak intensities showed that films with increasing deposition temperatures had higher degrees of crystallinity. XPS indicated that above 150 °C deposition temperatures, impurities in the film were reduced by ~4x. Higher deposition temperatures allow for increased adatom mobility, which can lead to higher densities and crystallinity, which are typically associated with lower wear rates. At deposition temperatures below 200 °C, precursor reactivity is sluggish and there is insufficient energy for complete surface reactions to occur, leading to film contamination and less dense films. The subtle differences in wear rates above 200 °C deposition temperature indicated that there are competing material properties that can either contribute to or detract from the wear behavior of the film, and a combination of desirable mechanical, physical, structural, and chemical properties are required for ultra-low wear rates to be achieved. The low wear and friction properties and low electrical resistivity of these films combined with the low deposition temperature, conformality, and atomic layer thickness control of PEALD make them potential candidates for applications such as thermally sensitive microelectronics and MEMS/NEMS.

1. Introduction

Titanium based metal nitride coatings (TiN) are widely used in commercial applications such as cutting tools, biomedical implants, aerospace components, and automotive parts due to their wear resistance, friction reducing properties, corrosion resistance, and high hardness [1–4]. These coatings are deposited using a variety of techniques including magnetron sputtering, physical vapor deposition, and

---

* Corresponding author. Department of Mechanical Engineering, Florida A&M University – Florida State University College of Engineering, Tallahassee, FL, 32310-5754, USA.
E-mail address: bkrick@eng.famu.fsu.edu (B.A. Krick).

https://doi.org/10.1016/j.wear.2023.204731
Received 19 September 2022; Received in revised form 11 November 2022; Accepted 17 November 2022

others. The addition of a third element to TiN such as vanadium (V), molybdenum (Mo), aluminum (Al), etc. to create ternary alloys is known to improve the wear rate and reduce the friction of the films [5–8]. Ternary alloys, Ti_xMo_yN [9–11] and Ti_xV_yN [12,13] reduce the coefficient of friction during dry sliding by forming lubricous oxides of Mo and V respectively. Ti_xV_yN also exhibits higher hardness and strength compared to its constituent binary nitrides which aids in wear reduction [14].

In recent years, TiVN films have been successfully deposited using plasma enhance atomic layer deposition (PEALD) and were found to be highly crystalline, dense films with low electrical resistivity [12]. Compared to other more conventional deposition methods, PEALD enables film deposition to occur at much lower temperatures [15,16]. Additionally, PEALD does not require line-of-sight for deposition, allowing for the creation of highly conformal films with atomic layer thickness control on complex surface features [17–19]. The low deposition temperature requirements combined with the atomic layer thickness control make these electrically conductive, thin (<100 nm) TiVN films a possible candidate for thermally sensitive microelectronics and MEMS/NEMS with complex surfaces and tight dimensional tolerance requirements [15,16].

While preliminary tribological testing of PEALD TiVN films has shown that these films can be ultralow wear ($K < 10^{-7}$ mm^3/Nm) and low friction ($\mu<0.3$), little is understood about the contribution of changing deposition parameters on the structure and resulting tribological properties of these films. Processing conditions such as substrate bias, partial gas pressure, deposition temperature, and elemental composition levels will impact the physical, structural, chemical, and mechanical properties of these films [14,20–22], which will directly influence the tribological behavior of the TiVN films. Improvements in the wear behavior of coatings have reportedly been brought about by crystallographic phase changes [23,24]. Wear rates also vary along specific crystallographic planes [23,25–28]. In order to form a fundamental understanding of the process-structure-property relationships of PEALD TiVN films, comprehensive analysis of resulting film structures and properties as a result of carefully controlled changes to processing parameters is needed.

In this study, $Ti_{0.5}V_{0.5}N$ films were deposited using plasma enhanced atomic layer deposition (PEALD). Varying the deposition temperature during ALD is one variable that affects film structure and composition. In previous works, ALD growth per cycle (GPC), crystallite size, crystallinity, and electrical resistivity of TiN and VN films were found to be affected by deposition temperature, even in fully saturated deposition conditions [29,30]. Higher deposition temperatures can increase the concentration of reaction sites depending on the reaction mechanisms [19,31], and increasing the growth temperature aids in enhancing crystallization by increasing adatom mobility [32]. High impurity concentrations at very low temperatures can hinder crystallization and result in amorphous films [32]. It can be argued that ALD introduces impurities in the film, but the use of plasma assisted ALD processes has also shown reduction in impurity concentration relative to purely thermal ALD [33–35]. In this work $Ti_xV_{1\text{-}x}N$ ($x \sim 0.5$) (henceforth referred to as TiVN for simplicity) films were deposited by PEALD on Si-thermal oxide substrates. Although the TiVN system has been extensively studied for sputtered films, the process-structure-property relationship of PEALD TiVN has yet to be fully understood. For this paper, the deposition temperatures of PEALD TiVN were varied from 150 °C to 350 °C with an increment of 50 °C. The effects of deposition temperature on the structural, chemical, physical, mechanical, and wear and friction properties of PEALD TiVN was investigated.

2. Materials and methods

2.1. Plasma enhanced atomic layer deposition (PEALD) growth

The PEALD TiVN films were deposited with a Veeco Fiji system equipped with a reactor turbo-molecular vacuum pump and variable conductance valve, a turbomolecular-pumped load lock, and a second generation (G2) style inductively coupled plasma source [36]. The TiVN films were achieved with a 1:1 alternating combination of established saturated, 250 °C Fiji TiN [30] and VN [29]processes. Tetrakis(dimethylamido) titanium (TDMAT) was used for the titanium precursor and tetrakis(dimethylamido) vanadium (TDMAV) was used for the vanadium precursor. The TDMAT and TDMAV precursors were both maintained at 75 °C. During precursor pulsing, 30 sccm of Ar carrier gas flows through the precursor manifold and 100/5 sccm of Ar/N_2 flows through the plasma source and the variable conductance valve is reduced to 22% to establish a reactor pressure of 200 mTorr. During the plasma steps, 10 sccm of Ar flows through the precursor manifold and 0/5sccm of Ar/N_2 flows through the plasma source and the variable conductance valve is fully opened resulting in a reactor pressure of 18 mTorr. The process starts with a VN cycle consisting of a 0.375s pulse of TDMAV, a 5 s purge, a 17.5s 300 W plasma, and a 10 s purge. The TiN cycle follows with a 0.25 s pulse of TDMAT, a 5 s purge, a 10 s 300 W plasma, and a 10 s purge. Gas flows and variable conductance valve settings were adjusted during the purges. A supercycle of TiVN consisted of one cycle of VN followed by one cycle of TiN. Growths of 750 supercycles were completed at substrate temperatures (deposition temperatures) of 150, 200, 250, 300, and 350 °C.

2.2. Friction and wear testing

Friction and wear testing of the TiVN thin films was performed using a sphere on flat testing configuration. A 3 mm diameter single crystal ruby (α-alumina) ball was slid against the TiVN thin film on a linearly reciprocating tribometer. Friction force and normal force were actively measured using a biaxial strain-gauge-based load cell mounted directly to the ruby ball fixture. The TiVN samples were mounted to a ball screw driven step servo stage which reciprocated the samples at a relatively slow sliding speed (1 mm/s) to minimize frictional heating of the material. Because TiVN films have been previously found to have high hardness, we aimed to use a countersurface material that would not wear during sliding against the TiVN films. A single crystal ruby (α-alumina) countersurface was selected due to its exceptionally high hardness and wear resistance. A normal load of 100 mN was selected in order to apply a Hertzian contact pressure of ~320 MPa between the ruby ball and the TiVN films, which is ~20-30x lower than reported hardness values for TiVN [22]. Stripe testing was performed at the following total sliding cycles and testing stroke lengths to evaluate the wear of the thin films: 500, 1.5k, 3k, 5k, 10k (10 mm, 8 mm, 6 mm, 4 mm, 2 mm) [34,37,38]. Samples were tested in air in a controlled environment at 30% RH and at room temperature.

$$K\left[mm^3/Nm\right] = \frac{V[mm^3]}{F_N[N]d[m]} = \frac{L[m]A[mm^2]}{F_N[N](2S[m/cycle]C[cycles])} = \frac{1000[mm\ cycles/m]A[mm^2]}{2F_N[N]C[cycles]} \qquad \text{(Eq. 1)}$$

To evaluate the wear rates of the samples, an optical profilometer was used to determine the surface profile of the wear scars. These films are on the order of 100 nm thick, so intact film wear scars are less than 100 nm deep. The specific wear rate K of the film was calculated using Equation (1). Traditionally, specific wear rate is calculated using the worn volume V divided by the applied normal load F_N and the total sliding distance d. Due to the very small thicknesses and worn volumes of the TiVN films, the surface profile of the wear scar collected through optical profilometry is used to calculate the wear rate of the films. The cross-sectional area of the wear scar is found by integrating the surface profile of the wear scar; the average of areas integrated from 30 line scans spaced periodically on the wear scar are reported as the worn area, A. The measured wear scar volume, V, is approximately equal to the average worn area, A times the wear scar length, L. The total sliding distance is equal to the product of two times the stroke ($2S$) and the total number of cycles, C. The reciprocating stroke length, S, has units of [m/cycle] in the denominator and is equal in magnitude to the length of the wear scar, L [m] in the numerator. This stroke length can be cancelled out, and using a unit conversion factor 1000 [mm cycles/m], the correct units of specific wear rate can be maintained [mm^3/Nm]. This leaves a final equation that is dependent on wear scar cross-sectional area A, normal load F_N, and sliding cycles C. Oddly, many papers in the literature attempt to calculate the wear rate in this way, but leave out the factor multiplying by 1000 to get the units correct, resulting in wear rates that are actually three orders of magnitude worse than the published values.

Friction and normal force were measured as a function of position for each reciprocation cycle, resulting in a friction loop. The friction force array was element-wise divided by the normal force array, to generate position-resolved friction coefficient data. From this friction coefficient data, a cycle friction coefficient was averaged over the middle 50% of the track length region, using both the forward and reverse reciprocation to offset transducer misalignment as in Ref. [39]. This results in a cycle friction coefficient and standard deviation of cycle friction for each sliding cycle.

2.3. X-ray diffraction (XRD) and X-ray reflectivity (XRR)

X-ray diffraction (XRD) and x-ray reflectivity (XRR) measurements were taken using a PANalytical Empyrean diffractometer with a Cu x-ray tube at a wavelength of 1.541 Å. For XRD measurements, a Bragg–-Brentano HD mirror with suitable slits were used to shape the incident beam to maximize irradiation on the sample. The diffracted beam was shaped with 7.5 mm antiscatter slit and a soller slit and detected with a PIXcel3D-Medipix3 1 × 1 area detector in scanning line 1D mode. Symmetric θ-2θ (gonio) scans were taken with a step size of 0.0066° and counting rate of 20.4 s/step.

The incident beam for XRR utilized a Bragg–Brentano HD mirror with a 1/8° fixed slit, 1/16° antiscatter slit, 4 mm mask and a soller slit. The diffracted beam was shaped with a 1/16° antiscatter slit and detected with a PIXcel3D-Medipix3 1 × 1 area detector in receiving mode with 1 of the 255 channels active having an active length of 0.055 mm. Symmetric θ-2θ (gonio) scans were taken within the range of 0–4° (2θ) with a step size of 0.005° (2θ) and a counting rate of 0.5 s/step. The XRR data were fitted to get estimates of mass density and thickness using X'Pert Reflectivity software (v 1.3a).

Grazing incidence x-ray diffraction (GIXRD) measurements utilized a Bragg–Brentano HD mirror with a 1/8° fixed slit, 1/8° antiscatter slit, 10 mm fixed mask and a soller slit to condition the incident beam. The diffracted beam was conditioned using a parallel plate collimator of 0.18° opening and a soller slit. The PIXcel3D-Medipix3 1 × 1 area detector used was in open detector mode with all of its 255 channels open having an active length of 14.025 mm. 2θ scans were taken for all measurements with the incident angle (ω) fixed at 1° with respect to the sample surface, with a step size of 0.04° and a counting rate of 5.5 s/step. For residual stress, each Bragg peak was scanned separately, and the counting rates were adjusted according to the relative peak intensity for ease of peak determination.

2.4. X-ray photoelectron spectroscopy (XPS)

X-ray photoelectron spectroscopy (XPS) measurements were collected using a Kratos Ultra-DLD system using monochromatic aluminum Kα radiation with an excitation energy of 1486.7 eV. High-resolution scans were collected using a step size of 0.1 eV and an appropriate number of scans to achieve suitable signal-to-noise ratios. Samples were sputtered for 30s using 200 eV Ar^+ ions to remove surface contamination prior to analysis. Compositional information was determined by fitting XPS data using CasaXPS software with appropriate relative sensitivity factors obtained from the instrument. Specific fitting and XPS analysis procedures are described previously elsewhere [12]. Peak locations were calibrated to the C1s peak energy for adventitious carbon at 284.8 eV.

2.5. Resistivity measurement with four-point probe

Film sheet resistance values were measured using a Lucas Labs 302 Resistivity Stand with a Keithley 2400 SourceMeter. Film resistivity values reported are the product of the four-point probe sheet resistance values and the x-ray reflectivity (XRR) film thickness estimates.

3. Results and discussion

3.1. Wear and friction

TiVN films deposited at a range of substrate temperatures (i.e., deposition temperatures, $T_{dep.}$) from 150 to 350 °C exhibited orders of magnitude of variation in wear rate (Fig. 1a). The TiVN 150 °C film had the highest wear rate of all samples tested, beginning with a wear rate of 4.5×10^{-6} mm^3/Nm, and rapidly increasing to total wear rates between 5-7 x 10^{-5} mm^3/Nm. The 200 °C, 300 °C, and 350 °C samples were remarkably similar in their wear performance over the course of testing up until 3k cycles, after which their behaviors diverged. At 5k cycles, the 200 °C sample wear rate begins to dip below the wear rates of the other two samples, reaching 1.2×10^{-6} mm^3/Nm. However, after 10k cycles, the wear rate jumps an order of magnitude to 2.9×10^{-5} mm^3/Nm. In comparison, the 300 °C sample total wear rate continues to decrease, reaching final wear rate of 1.1×10^{-6} mm^3/Nm. At 10k cycles, the 350 °C sample has a small uptick in its wear rate to 2.1×10^{-6} mm^3/Nm. The lowest wear rate sample overall was the TiVN deposited at 250 °C. The total wear rate of the sample was consistently ~ 2x lower than the rest of the low wear samples over the duration of testing. The 250 °C sample achieved a wear rate of 5.4×10^{-7} mm^3/Nm after 10k sliding cycles. Wear rates and relevant uncertainties are summarized in Table 1.

Comparing wear scar profile depths to film thickness shows that some films wore through and the thermal silicon oxide substrate began wearing as well. The 150 °C wear scar profiles indicate that while the sample had minor wear in the first 500 cycles, the film was completely worn through to the substrate after 1.5k cycles. This can be correlated to the friction data in Fig. 1b, where the friction coefficient of the 150 °C sample transitions from an initial friction coefficient of ~0.2 to a remarkably high and fluctuating friction coefficient (between 0.7 and 0.9). This high friction coefficient is indicative of the ruby ball countersurface rubbing against the thermal silicon oxide substrate.

The uptick in the wear rate, as well as the friction coefficient, of the 200 °C sample can also be correlated to the wear scar profile. Up until 5k sliding cycles, the total wear rate was continually decreasing with increasing sliding cycles. However, it is clear after 10k cycles that the film has been completely worn through to the substrate and the thermal oxide layer is being worn away. The 350 °C sample wear scar undergoes a similar wear rate uptick but to a much smaller extent, and the wear profile at 10k sliding cycles shows a region that has worn through to the substrate.

Films that had a continual decrease in total wear rate with increasing sliding cycles (250 °C, 300 °C) were not worn through into the substrate.

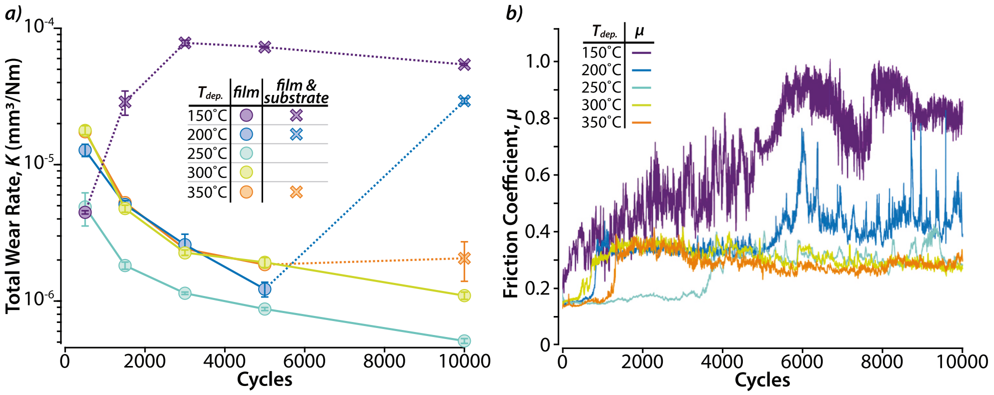

Fig. 1. a) Total specific wear rate over number of sliding cycles of TiVN films grown at deposition temperatures, $T_{dep.}$, from 150 to 350 °C on Si-Thermal Oxide. Dashed line indicates film has worn through to the substrate, and x data points indicate a combined film and substrate wear rate. Circle data points represent the wear rate of the ALD film that has not worn through to the substrate. b) Cycle friction coefficient of each film over total number of sliding cycles. It should be noted that as this is cycle-resolved friction data, the standard deviations of a cycle friction coefficient are much lower than the variations seen between cycles, thus the large variation and spikes in friction are signal and not noise.

Table 1

Wear rate, K [x10^{-6} mm^3/Nm] and uncertainty in wear rate, U_K results as a function of sliding cycles for each deposition temperature. Shaded cells indicate measurements that are thought to have worn through to the substrate.

	K [x10^{-6} mm^3/Nm] ± U_K				
Total Sliding Cycles	TiVN 150 °C	TiVN 200 °C	TiVN 250 °C	TiVN 300 °C	TiVN 350 °C
500	4.5 ± 0.1	13.5 ± 1.7	5.0 ± 0.3	17.9 ± 1.3	17 ± 0.8
1500	28.8 ± 5.8	5.1 ± 0.3	2.1 ± 0.4	4.8 ± 0.3	5.3 ± 0.3
3000	78.1 ± 3.7	2.6 ± 0.5	1.0 ± 0.1	2.3 ± 0.1	2.4 ± 0.1
5000	72.8 ± 1.1	1.2 ± 0.2	0.98 ± 0.08	1.9 ± 0.2	1.9 ± 0.1
10000	54.3 ± 0.9	29.3 ± 1.3	0.54 ± 0.07	1.1 ± 0.1	2.1 ± 0.7

In these cases, the wear scars continually grew deeper and wider over the course of testing without passing through to the substrate. It should be noted that some films were much thinner than others, as the 200 °C sample thickness was only 58 nm while the 300 °C sample was 95 nm. Based on these observations, it would be valuable to compare samples based on the best performance before wearing through the film for the low wear samples (excluding 150 °C).

After testing was concluded, the ruby ball countersurface was mapped using the scanning white light optical profilometer to observe any changes to the surface. For the films that were not worn completely through (250 °C and 300 °C), a patch of transferred debris was visible on the contacting surface of the ball. These patches at their widest were approximately the same width as the wear scar (∼20–40 μm), but with some variation in the width throughout their length (∼50%). The transferred material patch was ∼100–150 μm long with heights ranging from ∼50 to 500 nm (depending on the sample). Wear debris was also observed on the film in small piles at the ends of the stripe wear tracks and scattered along the edges of the wear tracks. The accumulation of the transferred material on the countersurface, or "transfer film", most likely contributed to changes in the shape of the wear tracks as well as changes in friction coefficient. The wear tracks have small grooves (<5 μm) inside the track and do not have a perfect circular segment cross sections. Their shape also appears to change over time/sliding cycles due to the evolving transfer film on the countersurface sliding against the film. This indicates a two-body grooving abrasive wear mechanism [40].

For films that wore through to the substrate over the course of testing, the ruby ball countersurface either had some transferred material with minor ball wear in the very center (350 °C), or they had significant ball wear due to prolonged contact with the Si-thermal oxide substrate (150 °C and 200 °C). The balls formed a flat spot that is slightly smaller than the width of the wear track, with debris/transferred material off to the sides. For the 200 °C sample, this spot was ∼40 μm wide, while the 150 °C sample had a flat spot that was ∼100 μm wide. According to the wear track line scans, the 200 °C film was worn through to the substrate somewhere between 5k and 10k total sliding cycles, while the 150 °C film was worn through between 500 and 1.5k cycles.

For all films, the wear scars appeared to have a non-uniform profile after only 500 sliding cycles, indicating initial transfer of debris to the ruby ball occurred very early during testing. The 250 °C sample had the shallowest initial wear scar, potentially due to a more stable initial transfer film formation. This could contribute to the 3-4x lower initial wear rate, followed by a continually decreasing total wear rate that was consistently lower than the other samples. The 200 °C sample also had an initially lower wear rate than the 300 °C and 350 °C sample. However, it quickly returned to nearly the same wear rate as the other samples. The wear behavior of these films and the differences observed between them are most likely due to a combination of transfer film formation and evolution during sliding as well as physical and structural differences in the films.

3.2. XPS

The atomic composition, as determined by XPS, of the PEALD TiVN films as a function of deposition temperature is shown in Fig. 2a. XPS fitting procedures for ALD TiVN thin films have been described in detail previously [12]. XPS results indicate that for all deposition temperatures, film composition is remarkably consistent, producing TiVN at all deposition conditions. That said, there are clear minor compositional differences in the films grown at different substrate temperatures (i.e., deposition temperatures). As the deposition temperature increases from 150 °C to 350 °C, the vanadium content of the films increases, at the expense of a reduction in both Ti and N content. Ti and V concentrations are equal at 200 °C, but higher growth temperatures promote V-rich films and the expense of some Ti content.

This trend is more clearly seen by plotting the N:Metal and Ti:V ratios as a function of deposition temperature, shown in Fig. 2b. Here, the N:Metal ratio is near 1.25 for TiVN films deposited at 150 °C, reducing to a near-ideal ratio of 1 at 350 °C. Simultaneously, the Ti:V ratio reduces from ∼1 at 150 °C to ∼0.8 at 350 °C, indicating again that increasing growth temperatures produce a more vanadium-rich film.

Fig. 2c shows that C contamination is just over 2% at 150 °C, but closer to 0.5% at temperatures above 150 °C. This reduction of C contamination indicates incomplete ALD ligand exchange reactions leading to residual carbon occurring at 150 °C deposition temperatures, while higher deposition temperatures lead to more complete ALD reactions. Oxygen concentration (Fig. 2c) shows the highest contamination levels just over 2.5% at 150 °C deposition temperatures, but this is reduced to ∼2% at temperatures over 250 °C, again indicative of incomplete ALD reactions occurring at 150 °C.

3.3. Growth per cycle

The growth per cycle (GPC) for TiVN films deposited on Si-thermal oxide substrates were calculated using the thickness estimates from

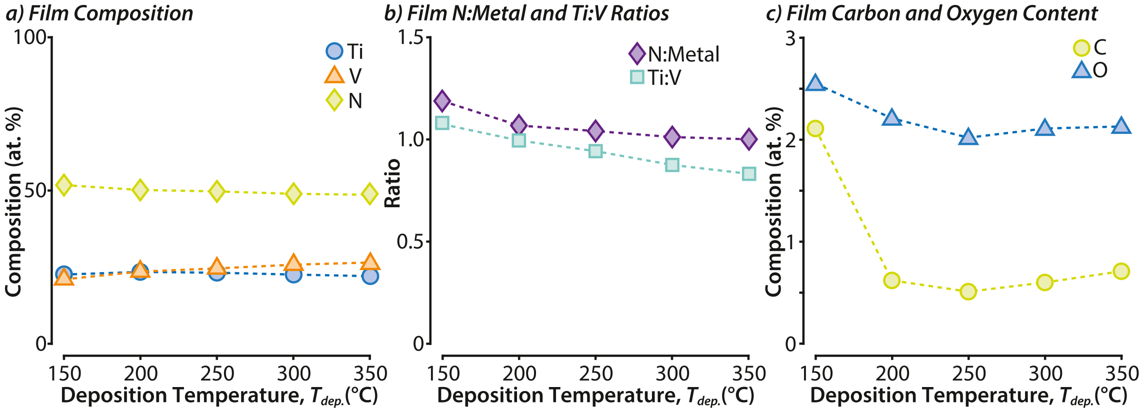

Fig. 2. a) The composition of the TiVN thin film is estimated from XPS measurement, b) the ratios of N:metal and Ti:V calculated, and c) the atomic % of O and C impurity found in the film at each deposition temperature ($T_{dep.}$).

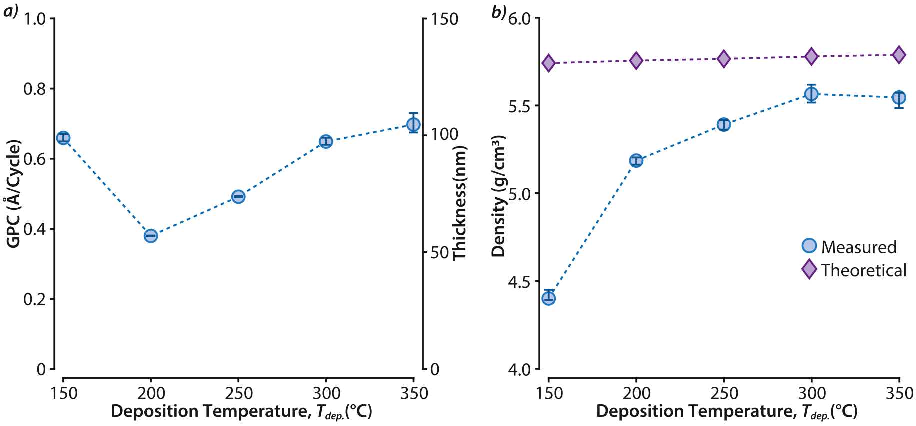

Fig. 3. Growth per cycle and film densities based on XRR experiments. a) GPC of TiVN thin films as a function of deposition temperature ($T_{dep.}$), calculated from XRR estimated film thickness for each N_2 plasma (or metal precursor) pulse. b) Calculated density of TiVN as a function of deposition temperature ($T_{dep.}$), compared with single crystal theoretical density of corresponding TiVN compositions based on XPS measurements.

the XRR fittings and plotted against the substrate temperature during deposition (Fig. 3a). GPC was calculated by dividing the average thickness of the film by the total number of metal or N_2 plasma pulses. The GPC increased monotonically from 0.38 to 0.7 Å/cycle as the temperature increased from 200 °C to 350 °C. The increase in GPC with temperature seen in our data can be attributed to either 1) an increase in reactive sites at higher temperature or 2) increased reactivity of either or both precursor at higher temperature [19,31,41–43]. A similar increase in GPC with temperature has been observed in previous works for both TiN and VN PEALD processes [29,30]. CVD behavior is unlikely, as the GPC would be expected to exhibit a much steeper increase with temperature along with non-uniformities in thickness.

At 150 °C the GPC observed was high relative to the 200 °C GPC. Although high growth rates at low temperatures occur due to the condensation of reactants on the reaction surface [19,44], the deposition temperature of 150 °C was well above the precursor temperature (75 °C) to avoid condensation. The TDMAT precursor decomposition was found to be slow below 205 °C by FTIR for CVD growth of TiN using TDMAT and N_2 [45]. Thus at 150 °C the TDMAT precursor may not have sufficient energy for surface reactions to occur. The incomplete reaction leaves ligands from the precursor causing high GPC. This theory can also be backed up by comparatively higher C impurity concentration found by XPS at 150 °C (Fig. 2c).

3.4. Density

The densities of the films were estimated from the fitting of XRR data and are plotted against the film deposition temperature(Fig. 3b). The theoretical density (Fig. 3b) was calculated from the weighted average of the bulk density of cubic TiN and cubic VN based on the XPS composition. At 150 °C, the incomplete surface reactions leave low-density organic species that contribute to lowering the film density [45]. Other contributing factors such as disorder in the crystal lattice as well as increased porosity are likely factors in the lower film density. With increasing deposition temperature, the densities of the films increase and saturate at 250 °C as the surface reactions presumably go toward completion. The high densities obtained at higher temperatures (200–350 °C) are still 4–8% lower than the theoretical values since the films contain impurities (C, O) and are nanocrystalline with an abundance of grain boundaries that introduce disorder in the structure and lower the density below the theoretical values.

3.5. Crystal structure

The films were found to be polycrystalline at all deposition temperatures, evident by the x-ray diffraction (XRD) measurements (Fig. 4a). Grazing incidence XRD (GIXRD) of the TiVN films shows peaks near 36.8°, 42.8°, 62.5°, 75°, 79°, 106.5° and 111° that correspond to the (111), (200), (220), (311), (222), (331) and (420) planes respectively, of an FCC rock salt crystal structure with space group $Fm\overline{3}m$ and space group number 225 (Fig. 4a). All the observed peaks were located between the reference peak locations for FCC TiN (00-038-1420) and FCC VN (01-073-0528), suggesting a single-phase solid solution between cubic TiN and cubic VN. The smaller V^{3+} ion replaces the Ti^{3+} ion in the

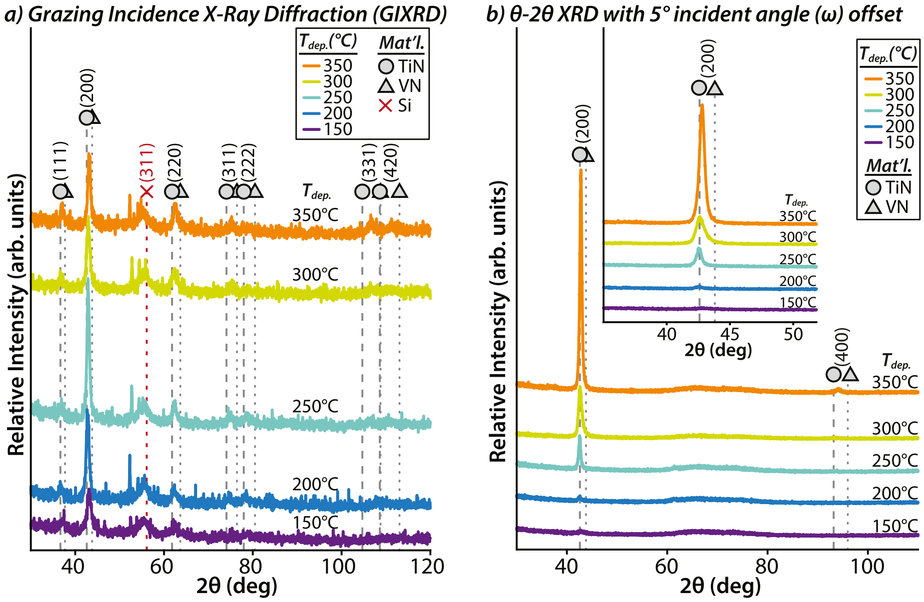

Fig. 4. a) Grazing incidence x-ray diffraction of TiVN thin films with peaks labeled for rock salt TiN (circles), rock salt VN (triangles) and Si substrate (red x). b) θ-2θ X-ray diffraction measured with a 5° offset to the incident angle (ω) to avoid detecting large substrate signals. Preferential orientation towards (100) is evident by the detection of (200) and (400) planes only. The (200) peak is enlarged in the inset to have better view for the changes in the intensity with deposition temperature ($T_{dep.}$). (For interpretation of the references to colour in this figure legend, the reader is referred to the Web version of this article.)

TiN lattice, effectively reducing the lattice spacing and increasing the 2θ values of the Bragg reflections. TiN films deposited at 150–350 °C by thermal ALD, using alkylamide precursors and NH_3, generally tend to be amorphous or weakly crystalline [32,46–48]. The use of PEALD with alkylamide precursors has shown evidence of crystalline films [12,29,33,34,49], although amorphous structures have also been reported [50].

Increase in deposition temperature can also enhance crystal quality in a direct fashion by allowing atoms to occupy equilibrium positions during ALD cycles, or indirectly by reducing impurity concentration at elevated deposition temperatures [32]. A closer look at the θ-2θ XRD scans of polycrystalline TiVN films reveals the sudden increase or appearance of Bragg peak intensity beyond 150 °C deposition temperatures (Fig. 4b), which coincides with the dramatic decrease in C concentration beyond 150 °C (Fig. 2b). The θ-2θ XRD scans also reveal that the polycrystalline films grew with a <100> preferred orientation. With increasing temperature, the Bragg peak intensity increases, suggesting better crystallinity due to enhanced mobility of atoms on the growth surface. Thus, the increase in deposition temperature improved the crystallinity of the TiVN films. Additionally, the (200) plane grew preferentially out of plane with a lattice spacing of ~2.14 Å. The GPC of 0.38–0.70 Å/cycle suggests, on average, it took 3 to 5 cycles to deposit a monolayer based on the out of plane direction being dominated by [200]. This suggests self-limiting ALD behavior and rules out CVD, where much higher GPC, along with non-uniformities in the film thickness, would be expected.

The apparent crystallite sizes were estimated from the full width at half maximum (FWHM) of the (200) peak from the GIXRD data, using the Debye-Scherrer equation, considering crystallite size to be the only source of broadening. The diffraction data was not corrected for instrumental broadening or microstrain. The purpose of the crystallite size quantification is to determine the trend between samples. The calculated crystallite sizes hovered between 12.4 and 14.9 nm with minor changes for the films deposited at 200–350 °C. For the 150 °C sample, the calculated crystallite size was 6.8 nm, which may be because of broadening from the retained organic ligands from the precursor and does not necessarily represent the physical size of the crystallite. It should be noted that the crystallite sizes calculated are not limited by the film thickness; the crystallite sizes reported are approximately 5 – 8x smaller than the film thicknesses. Similar values of crystallite sizes were also found for TiMoN deposited by PEALD using identical growth conditions [33,34].

The lattice parameter of TiVN was calculated from all the observable Bragg peaks of the GIXRD and plotted as a function of deposition temperature (Fig. 5a). No significant difference in the lattice parameter was

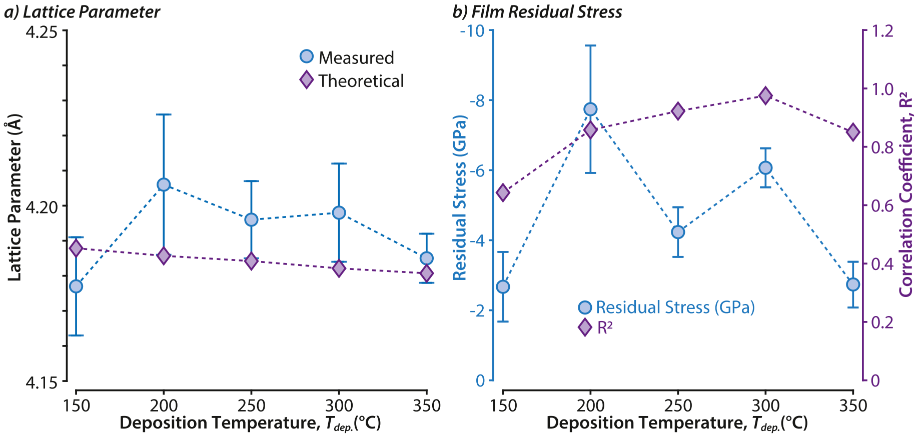

Fig. 5. a) The average lattice parameter from all the observable Bragg peaks for each deposition temperature compared to the theoretical lattice parameter of a stress free TiVN crystal structure of corresponding composition. b) Residual stress of TiVN thin film calculated from GIXRD using $\sin^2\psi$ method showing compressive residual stress at all deposition temperatures ($T_{dep.}$).

observed with increasing deposition temperature as is expected since the composition of the films did not change significantly. At all deposition temperatures, the lattice parameters were found to be slightly higher than the theoretical value which was calculated considering a solid solution between TiN (00-038-1420) and VN (01-073-0528) based on the XPS composition. The difference between the theoretical and measured lattice parameter is between 0.10 and 0.48%. This deviation from the theoretical value could be due to the impurity elements present in the films and the abundance of grain boundaries.

3.6. *Residual stress*

The residual film stress was calculated from the lattice strain measured by the deviation in d-spacing measured from the GIXRD data using the $\sin^2\psi$ method [51]. The lattice strain of the (111), (200), (220), (311), (222), (331) and (420) planes were considered for the calculation. The 2θ positions for each peak were determined using a parabolic approach to minimize error in stress calculations [52]. Since the elastic moduli (E) of TiN and VN are anisotropic, the value of E would be different for different planes and was calculated using the following equations [53,54].

$$E_{hkl} = S_{11} - 2\left(S_{11} - S_{12} - \frac{S_{44}}{4}\right)\left(\frac{h^2k^2 + k^2l^2 + l^2h^2}{\left(h^2 + k^2 + l^2\right)^2}\right) \tag{Eq. 2}$$

$$S_{11} = \frac{C_{11} + C_{12}}{(C_{11} - C_{12})(C_{11} + 2C_{12})} \tag{Eq. 3}$$

$$S_{12} = \frac{-C_{12}}{(C_{11} - C_{12})(C_{11} + 2C_{12})} \tag{Eq. 4}$$

$$S_{44} = \frac{1}{C_{44}} \tag{Eq. 5}$$

Here E_{hkl} is the elastic modulus of *hkl* plane, S_{ij} is the elastic compliance and C_{ij} is the elastic constant. For TiN, 640, 115 and 159 GPa were used as C_{11}, C_{12} and C_{44} respectively [55]. For VN, 680, 140 and 139 GPa were used as C_{11}, C_{12} and C_{44} respectively [55]. The E_{hkl} for TiVN for each *hkl* plane was considered to be the weighted average of the E_{hkl} of TiN and VN based on the Ti:V determined from XPS. The Poisson's ratio (ν) for both TiN and VN were determined from the elastic constants using the following equation [56]:

$$\nu = \frac{C_{12} - \frac{H}{5}}{2\left(C_{12} + C_{44} - \frac{2H}{5}\right)} \tag{Eq. 6}$$

Here $H\ (= 2C_{44} + C_{12} - C_{11})$ is the anisotropic factor of the crystal. The Poisson's ratio was also considered as the weighted average for TiVN. The details of the biaxial stress model to calculate the residual stress is explained elsewhere [51].

The residual stresses of the TiVN films were calculated from the GIXRD data. At all deposition temperatures, the films were found to be under compressive stresses between 2.7 and 7.7 GPa. Total stresses in thin films can be expressed according to the following equation [57].

$$\sigma_{tot} = \sigma_{ext} + \sigma_{th} + \sigma_i \tag{Eq. 7}$$

Here, σ_{ext} is the stress due to external loading and is not a concern here since the films were not under loading during stress measurements. σ_{th} is the thermal stress due to mismatch in thermal expansion between the film and the substrate upon cooling from the deposition temperature to room temperature [58]. σ_i is the intrinsic stress developed during deposition due to bombardment by high energy plasma [58]. The thermal expansion coefficient for the film is approximately one order of magnitude higher than the Si substrate [59–61]. As a result, the film contracts more than the substrate during cooling from the deposition temperature causing a tensile thermal stress. Therefore, it can be concluded that the magnitude of the compressive internal stress developed during deposition is higher than the total residual stress measured as depicted in Fig. 5b.

The intrinsic stress developed during deposition is a result of a balance between multiple stress generation and relaxation mechanisms [62]. Compressive stress in continuous thin films can arise due to the process of insertion of atoms in the grain boundary driven by either entropy or kinetics [63–65]. The large quantity of grain boundaries available in the TiVN films due to the nanosized grains contributes to the generation of compressive stresses in the films. Atomic peening due to bombardment by N_2 plasma ions can also cause compressive stress in the films [66,67]. Lattice distortion brought about by the substitution of Ti with V and the entrapment of impurity atoms can also cause compressive stresses [62].

3.7. *Resistivity*

Electrical resistivity was found to be very high in the 150 °C sample (~1860 μΩ-cm), nearly 10-20x greater than the resistivity measured for the 200–350 °C samples (Fig. 6). The lower density coupled with the much higher levels of impurities found in the 150 °C samples are causes for this high measured resistivity due to the scattering of charge carriers from the defects [68]. The low resistivity values measured for the 200–350 °C samples ranged from 100 to 200 μΩ-cm and were found to decrease with increasing temperature. This decrease can be correlated to lower impurity levels and higher densities found in the higher deposition temperature samples.

4. Material property and wear behavior discussion

Variation of deposition temperature during PEALD of TiVN films was found to change film structure and properties, such as crystallite size, density, crystallinity, GPC, and impurity content. Wear behavior was also found to differ based on film deposition temperature. This variation in wear could be attributed to the culmination of changes experienced in the structure and properties of the films themselves, as the wear behavior is typically dependent on multiple factors simultaneously.

The nearly 2x variation in GPC observed over the deposition temperature range led to film thicknesses ranging from as small as 58 nm to as large as 106 nm. This proved challenging when attempting to evaluate the wear rates of the films, as some films wore through to the substrate before 10k sliding cycles could be completed. For example, the

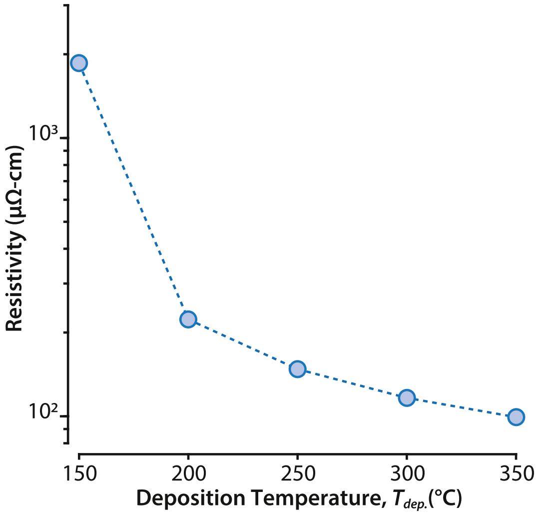

Fig. 6. Electrical resistivity of the TiVN films calculated from sheet resistance measured by four-point probe and film thickness estimated from XRR for all deposition temperatures ($T_{dep.}$).

200 °C sample (58 nm thick) wore through to the substrate prior to 10k sliding cycles despite having the second lowest wear rate prior to film failure. In contrast, the 250 °C and 300 °C samples never wore completely through and were able to maintain low wear rates. While the 150 °C sample had one of the highest growth rates and thickest films (99 nm), other film properties led to extremely high wear rates and delamination after the first 500 sliding cycles, wearing through the film completely.

High density (close to theoretical) and high compressive stresses are desirable in multi-metal nitride thin films, as they increase the wear/scratch resistance of the film. High compressive stresses inhibit crack formation and close cracks forming at the sliding interface. High density films are typically harder and more wear resistant, especially when voids are minimized. In these films, the highest compressive stresses were seen in the 200 °C (−7.7 GPa) and 300 °C (−6 GPa) samples. The 250 °C had moderate compressive stresses in comparison (−4.2 GPa), while the 150 °C and 350 °C samples had the lowest (−2.7 GPa). While high compressive stresses can be advantageous for wear behavior, if the stresses are too high or other material properties like density are lower than desired, the films can actually be negatively affected by these high compressive stresses [69]. In the case of the 150 °C sample, the measured density was ~23% lower than the calculated theoretical density. Compared to the films deposited at higher temperatures, the 150 °C sample has four times as much C % due to retained ligands from the precursor. On top of the relative density differences of carbon, the retained ligands block reaction at coordination sites of the Ti and V metal precursor, resulting in more disorder in the crystal lattice and possibly porosity. Additionally, the simple thermodynamics perspective suggests that lower temperature growths are more likely to have disorder in the crystal lattice and porosity. Additionally, ALD films deposited at lower temperatures near 150 °C are known to contain considerable residual hydrogen, in some cases over 10%, which can contribute significantly to lowered film densities [70]. The low density and low crystallinity, combined with high residual stresses could result in higher wear rates observed in the 150 °C sample [34].

For samples with deposition temperatures between 200 °C and 350 °C, the carbon impurity content was 4x lower than the 150 °C sample, and consequently the density and crystallinity (Bragg peak intensity) is higher. Samples in the 250–350 °C range had comparable densities that were within ~5% of the calculated theoretical density. As mentioned previously, these samples had a wide variation in compressive stresses, and stresses as high as −7.7 GPa. While the compressive stresses do not appear to correlate to wear rate, it is possible that there is an ideal stress state for these films to promote low wear. A tradeoff in compressive stresses might exist where films need a high enough residual stresses to reduce wear [69], yet too high of residual stresses can lead to coating fracture and delamination.

In many materials, decreasing grain size leads to an increase in hardness and strength, known as Hall-Petch behavior [71]. This increase in hardness can be advantageous for wear behavior. Archard's Wear equation states that wear is inversely proportional to the hardness of the softer of the two materials in a sliding pair [72]. While this equation has limitations, this relationship has been shown to hold for nanocrystalline metals and other metal nitrides, with increasing hardness correlating to decreasing wear [73–75]. However, when grain sizes in nanocrystalline materials are below certain thresholds, inverse Hall-Petch behavior can be observed [75]. In works by Qui et al., inverse Hall-Petch behavior was observed in grain sizes smaller than 19-14 nm in ZrN films, where decreasing grain size led to lower hardness. In the case of the TiVN films, crystallize sizes were found to increase from ~6 nm (150 °C) to ~15 nm (250 °C), after which the size decreased to ~12 nm (350 °C). The 250 °C sample exhibited wear rates 2x lower than the 200, 300, and 350 °C samples, all of which had comparable grain size values. If the nanocrystalline TiVN film experiences inverse Hall-Petch behavior in this region of crystallite size, it is possible that the slightly higher crystallite size in the 250 °C sample caused a minor increase in film hardness, leading to marginal (2x) improvements in wear rate.

The subtle differences in wear rates above 200 °C deposition temperature indicate that there are competing material properties that can either contribute to or detract from the wear behavior of the film, and a combination of desirable mechanical, physical, structural, and chemical properties are required for ultra-low wear rates to be achieved. It appears that density plays a primary role in the wear behavior of these films, with the low-density film (150 °C) exhibiting extremely poor wear performance, while wear rates of all other samples were more closely grouped. From a wear mechanism perspective, the evolving transfer film formation during testing can affect the two-body groove abrasive wear observed in the samples. The small variations in wear rate of the films (≥200 °C) are most likely impacted by initial transfer film formation and stabilization combined with the intrinsic characteristics of the films.

5. Conclusion

The wear behavior, mechanical, physical, structural, and chemical properties of PEALD TiVN films were found to vary significantly with film deposition temperature. At a deposition temperature of 150 °C, the film was found to have the lowest density, lowest degree of crystallinity, highest levels of impurity, highest resistivity, and the highest wear rate of all the films, with the film wearing through completely to the substrate within the first 1000 sliding cycles. At this deposition temperature, it is difficult for complete surface reactions to occur due to insufficient energy and low adatom mobility, which creates a low-density film with excess carbon content. However, when deposition temperatures are 200 °C or higher, increased adatom mobility creates high density, highly crystalline films. These physical properties contributed to the low wear rates of samples above 200 °C, with 250 °C sample reaching the lowest wear rate of 5.4×10^{-7} mm^3/Nm. While the specific mechanisms behind the small variation in wear rate of samples in the 200–350 °C range are not fully understood, it is clear that the wear behavior is dependent on a variety of competing physical, chemical, structural, and mechanical properties, as well as transfer film formation and stabilization.

Declaration of competing interest

The authors declare that they have no known competing financial interests or personal relationships that could have appeared to influence the work reported in this paper.

Acknowledgements

All the authors acknowledge the National Science Foundation for providing funding for this research through the project NSF No. CMMI #1826251. This material is based upon work supported by the National Science Foundation Graduate Research Fellowship Program under Grant #1449440 (Van Meter) and #1842163 (Babuska).

References

[1] K.V. Chauhan, S.K. Rawal, A review paper on tribological and mechanical properties of ternary nitride based coatings, Procedia Technol 14 (2014) 430–437, https://doi.org/10.1016/j.protcy.2014.08.055.

[2] X.H. Zhang, D.X. Liu, H.B. Tan, X.F. Wang, Effect of TiN/Ti composite coating and shot peening on fretting fatigue behavior of TC17 alloy at 350 °C, Surf. Coating. Technol. 203 (16) (May 2009) 2315–2321, https://doi.org/10.1016/j.surfcoat.2009.02.058.

[3] C. Lorenzo-Martin, O. Ajayi, A. Erdemir, G.R. Fenske, R. Wei, Effect of microstructure and thickness on the friction and wear behavior of CrN coatings, Wear 302 (1–2) (Apr. 2013) 963–971, https://doi.org/10.1016/j.wear.2013.02.005.

[4] B. Wendler, Vacuum annealing studies of the structure and of mechanical properties of thin titanium nitride films deposited by activated reactive evaporation, Thin Solid Films 141 (2) (Aug. 1986) 223–228, https://doi.org/10.1016/0040-6090(86)90350-0.

[5] H.C. Barshilia, K.S. Rajam, Raman spectroscopy studies on the thermal stability of TiN, CrN, TiAlN coatings and nanolayered TiN/CrN, TiAlN/CrN multilayer coatings (2020), https://doi.org/10.1557/JMR.2004.0444.

[6] Q. Luo, P.E. Hovsepian, Transmission electron microscopy and energy dispersive X-ray spectroscopy on the worn surface of nano-structured TiAlN/VN multilayer coating, Thin Solid Films 497 (1–2) (Feb. 2006) 203–209, https://doi.org/10.1016/j.tsf.2005.10.086.

[7] W. Gulbiński Tomaszewski, A. Urbanowicz, T. Suszko, A. Lewandowski, W. Gulbiński, TiAlN based wear resistant coatings modified by molybdenum addition, Vacuum 121 (Nov. 2015) 223–229, https://doi.org/10.1016/j.vacuum.2015.08.027.

[8] D.B. Lewis, et al., The effect of (Ti+Al):V ratio on the structure and oxidation behaviour of TiAlN/VN nano-scale multilayer coatings, Surf. Coating. Technol. 177–178 (Jan. 2004) 252–259, https://doi.org/10.1016/j.surfcoat.2003.09.041.

[9] J.W. Jeon, S.G. Hong, K.R.H.R. Kim, K.R.H.R. Kim, Synthesis and characteristics of new quaternary Ti–Mo–Si–N coatings by a hybrid coating system, J. Vac. Sci. Technol. A Vacuum, Surfaces, Film. 26 (1) (Jan. 2008) 140–145, https://doi.org/10.1116/1.2821730.

[10] J. Xu, H. Ju, L. Yu, Influence of silicon content on the microstructure, mechanical and tribological properties of magnetron sputtered Ti–Mo–Si–N films, Vacuum 110 (Dec. 2014) 47–53, https://doi.org/10.1016/j.vacuum.2014.08.010.

[11] Q. Yang, L.R. Zhao, P.C. Patnaik, X.T. Zeng, Wear resistant TiMoN coatings deposited by magnetron sputtering, Wear 261 (2) (Jul. 2006) 119–125, https://doi.org/10.1016/j.wear.2005.07.008.

[12] M.J. Sowa, et al., Plasma-enhanced atomic layer deposition of titanium vanadium nitride, J. Vac. Sci. Technol., A 36 (6) (2018), 06A103, https://doi.org/10.1116/1.5037463.

[13] Y.-Y.Y. Chang, H. Chang, L.-J.J. Jhao, C.-C.C. Chuang, Tribological and mechanical properties of multilayered TiVN/TiSiN coatings synthesized by cathodic arc evaporation, Surf. Coating. Technol. 350 (January) (Sep. 2018) 1071–1079.

[14] B.A. Latella, B.K. Gan, K.E. Davies, D.R. McKenzie, D.G. McCulloch, Titanium nitride/vanadium nitride alloy coatings: mechanical properties and adhesion characteristics, Surf. Coating. Technol. 200 (11) (Mar. 2006) 3605–3611, https://doi.org/10.1016/j.surfcoat.2004.09.008.

[15] T.M. Mayer, J.W. Elam, S.M. George, P.G. Kotula, R.S. Goeke, Atomic-layer deposition of wear-resistant coatings for microelectromechanical devices, Appl. Phys. Lett. 82 (17) (Apr. 2003) 2883–2885, https://doi.org/10.1063/1.1570926.

[16] N. Ouldhamadouche, et al., Electrodes based on nano-tree-like vanadium nitride and carbon nanotubes for micro-supercapacitors, J. Mater. Sci. Technol. 34 (6) (Jun. 2018) 976–982, https://doi.org/10.1016/j.jmst.2017.11.048.

[17] R.L. Puurunen, Surface chemistry of atomic layer deposition: a case study for the trimethylaluminum/water process, J. Appl. Phys. 97 (12) (Jun. 2005), 121301, https://doi.org/10.1063/1.1940727. American Institute of PhysicsAIP.

[18] R.W. Johnson, A. Hultqvist, S.F. Bent, A brief review of atomic layer deposition: from fundamentals to applications, Mater. Today 17 (5) (Jun. 2014) 236–246, https://doi.org/10.1016/j.mattod.2014.04.026. Elsevier B.V.

[19] S.M. George, Atomic layer deposition: an overview, Chem. Rev. 110 (1) (Jan. 2010) 111–131, https://doi.org/10.1021/cr900056b.

[20] F.F. Klimashin, N. Koutná, H. Euchner, D. Holec, P.H. Mayrhofer, The impact of nitrogen content and vacancies on structure and mechanical properties of Mo-N thin films, J. Appl. Phys. 120 (18) (Nov. 2016), https://doi.org/10.1063/1.4966664.

[21] N.K. Ponon, et al., Effect of Deposition Conditions and Post Deposition Anneal on Reactively Sputtered Titanium Nitride Thin Films, 2015, https://doi.org/10.1016/j.tsf.2015.02.009.

[22] C. Montero-Ocampo, E.A. Ramírez-Ceja, J.A. Hidalgo-Badillo, Effect of codeposition parameters on the hardness and adhesion of TiVN coatings, Ceram. Int. 41 (9) (Nov. 2015) 11013–11023.

[23] T. Nakano, et al., Orientation dependence of the wear resistance in the Co–Cr–Mo single crystal, Wear 478–479 (Aug. 2021), 203758, https://doi.org/10.1016/J.WEAR.2021.203758.

[24] A. Ziębowicz, K. Matus, W. Pakieła, G. Matula, M. Pawlyta, Comparison of the crystal structure and wear resistance of Co-based alloys with low carbon content manufactured by selective laser sintering and powder injection molding, Crystals 10 (3) (Mar. 2020) 197, https://doi.org/10.3390/CRYST10030197, 2020, Vol. 10, Page *197*.

[25] G. Zeng, W. Sun, R. Song, N. Tansu, B.A. Krick, Crystal orientation dependence of gallium nitride wear, Sci. Rep. 7 (1) (2017) 1–6, https://doi.org/10.1038/s41598-017-14234-x.

[26] B.S. El-Dasher, et al., Crystallographic anisotropy of wear on a polycrystalline diamond surface, Appl. Phys. Lett. 88 (24) (Jun. 2006), 241915, https://doi.org/10.1063/1.2213180.

[27] S. Spanou, E.A. Pavlatou, Ni/nano-TiO2 composite electrocoatings: correlation between structural characteristics microhardness and wear resistance, in: Zeitschrift Fur Physikalische Chemie, 225, Mar. 2011, pp. 313–324, https://doi.org/10.1524/zpch.2011.0052, 3.

[28] D. Kumar, N.N. Gosvami, J. Jain, Influence of crystallographic orientation on nanoscale friction and wear mechanisms of the AZ91 alloy, Tribol. Lett. 68 (3) (Aug. 2020) 1–10, https://doi.org/10.1007/S11249-020-01330-9, 2020 683.

[29] A.C. Kozen, et al., Plasma-enhanced atomic layer deposition of vanadium nitride, J. Vac. Sci. Technol., A 37 (6) (Oct. 2019), 061505, https://doi.org/10.1116/1.5109671.

[30] I. Krylov, et al., Obtaining low resistivity (~100 μΩ cm) TiN films by plasma enhanced atomic layer deposition using a metalorganic precursor, J. Vac. Sci. Technol. A Vacuum, Surfaces, Film. 36 (5) (Jul. 2018), 051505, https://doi.org/10.1116/1.5035422.

[31] H.H. Sønsteby, A. Yanguas-Gil, J.W. Elam, Consistency and reproducibility in atomic layer deposition, J. Vac. Sci. Technol., A 38 (2) (Mar. 2020), 020804, https://doi.org/10.1116/1.5140603.

[32] V. Miikkulainen, M. Leskelä, M. Ritala, R.L. Puurunen, Crystallinity of inorganic films grown by atomic layer deposition: overview and general trends, J. Appl. Phys. 113 (2) (Jan. 2013), 021301, https://doi.org/10.1063/1.4757907.

[33] M.I. Chowdhury, et al., Plasma enhanced atomic layer deposition of titanium nitride-molybdenum nitride solid solutions, J. Vac. Sci. Technol., A 39 (1) (Jan. 2021), 012407, https://doi.org/10.1116/6.0000717.

[34] M.I. Chowdhury, et al., Plasma-enhanced atomic layer deposition of titanium molybdenum nitride: influence of RF bias and substrate structure, J. Vac. Sci. Technol. A Vacuum, Surfaces, Film. 39 (5) (Aug. 2021), 053408, https://doi.org/10.1116/6.0001175.

[35] H. Van Bui, et al., Initial growth, refractive index, and crystallinity of thermal and plasma-enhanced atomic layer deposition AlN films, J. Vac. Sci. Technol. A Vacuum, Surfaces, Film. 33 (1) (Oct. 2014), 01A111, https://doi.org/10.1116/1.4898434.

[36] M.J. Sowa, Role of plasma enhanced atomic layer deposition reactor wall conditions on radical and ion substrate fluxes, J. Vac. Sci. Technol., A 32 (1) (Nov. 2013), https://doi.org/10.1116/1.4831896.

[37] K.L. Harris, et al., PTFE tribology and the role of mechanochemistry in the development of protective surface films, ACS Macromol 48 (2015), https://doi.org/10.1021/acs.macromol.5b00452.

[38] A.A. Pitenis, et al., Ultralow wear PTFE and alumina composites: it is all about tribochemistry, Tribol. Lett. 57 (1) (2015), https://doi.org/10.1007/s11249-014-0445-6.

[39] D.L. Burris, W.G. Sawyer, Addressing practical challenges of low friction coefficient measurements, Tribol. Lett. 35 (1) (Jul. 2009) 17–23, https://doi.org/10.1007/s11249-009-9438-2.

[40] G. Zeng, N. Tansu, B.A. Krick, Moisture dependent wear mechanisms of gallium nitride, Tribol. Int. 118 (2018) 120–127, https://doi.org/10.1016/j.triboint.2017.09.018.

[41] Y.C. Jung, et al., Low temperature thermal atomic layer deposition of aluminum nitride using hydrazine as the nitrogen source, Materials 13 (15) (Jul. 2020) 3387, https://doi.org/10.3390/ma13153387.

[42] S.B. Kim, X. Zhao, L.M. Davis, A. Jayaraman, C. Yang, R.G. Gordon, Atomic layer deposition of tin monosulfide using vapor from liquid bis(N, N′-diisopropylformamidinato)tin(II) and H2S, ACS Appl. Mater. Interfaces 11 (49) (Dec. 2019) 45892–45902, https://doi.org/10.1021/acsami.9b16933.

[43] E. Østreng, O. Nilsen, H. Fjellvåg, Optical properties of vanadium pentoxide deposited by ALD, J. Phys. Chem. C 116 (36) (Sep. 2012) 19444–19450, https://doi.org/10.1021/jp304521k.

[44] W. Jang, et al., Temperature dependence of silicon nitride deposited by remote plasma atomic layer deposition, Phys. Status Solidi 211 (9) (Sep. 2014) 2166–2171, https://doi.org/10.1002/pssa.201431162.

[45] J.P.A.M. Driessen, J. Schoonman, K.F. Jensen, Infrared spectroscopic study of decomposition of Ti(N(CH[sub 3])[sub 2])[sub 4], J. Electrochem. Soc. 148 (3) (2001) G178, https://doi.org/10.1149/1.1350687.

[46] J.-H. Yun, E.-S. Choi, C.-M. Jang, C.-S. Lee, Effect of post-treatments on atomic layer deposition of TiN thin films using tetrakis(dimethylamido)titanium and ammonia, Jpn. J. Appl. Phys. 41 (4A) (Apr. 2002) L418, https://doi.org/10.1143/JJAP.41.L418.

[47] F. Fillot, et al., Investigations of titanium nitride as metal gate material, elaborated by metal organic atomic layer deposition using TDMAT and NH3, Microelectron. Eng. 82 (3–4 SPEC. ISS) (2005) 248–253, https://doi.org/10.1016/j.mee.2005.07.083.

[48] J.W. Elam, M. Schuisky, J.D. Ferguson, S.M. George, Surface chemistry and film growth during TiN atomic layer deposition using TDMAT and NH3, Thin Solid Films 436 (2) (Jul. 2003) 145–156, https://doi.org/10.1016/S0040-6090(03)00533-9.

[49] P. Caubet, et al., Low-temperature low-resistivity PEALD TiN using TDMAT under hydrogen reducing ambient, J. Electrochem. Soc. 155 (8) (Jun. 2008) H625, https://doi.org/10.1149/1.2940306.

[50] J.Y. Kim, D.Y. Kim, H.O. Park, H. Jeon, Characteristics and compositional variation of TiN films deposited by remote PEALD on contact holes, J. Electrochem. Soc. 152 (1) (Nov. 2004) G29, https://doi.org/10.1149/1.1825913.

[51] A. Nezu, H. Matsuzaka, R. Yokoyama, A current perspective of the state-of-the-art in stress analysis Technical articles, Rig J 30 (2) (2014) 4.

[52] Q. Luo, A.H. Jones, High-precision determination of residual stress of polycrystalline coatings using optimised XRD-sin2ψ technique, Surf. Coating. Technol. 205 (5) (Nov. 2010) 1403–1408, https://doi.org/10.1016/J.SURFCOAT.2010.07.108.

[53] J.M. Zhang, Y. Zhang, K.W. Xu, V. Ji, Young's modulus surface and Poisson's ratio curve for cubic metals, J. Phys. Chem. Solid. 68 (4) (Apr. 2007) 503–510, https://doi.org/10.1016/J.JPCS.2007.01.025.

[54] M. Rabiei, et al., Measurement modulus of elasticity related to the atomic density of planes in unit cell of crystal lattices, Materials 13 (19) (Oct. 2020) 4380, https://doi.org/10.3390/ma13194380.

[55] D. Edström, D.G. Sangiovanni, L. Hultman, V. Chirita, Effects of atomic ordering on the elastic properties of TiN- and VN-based ternary alloys, Thin Solid Films 571 (P1) (2014) 145–153, https://doi.org/10.1016/j.tsf.2014.09.048.

[56] L. Liu, X.Z. Wu, R. Wang, H.F. Feng, S. Wu, High-pressure effect on elastic constants, stacking fault energy and correlation with dislocation properties in MgO and CaO, Eur. Phys. J. B 85 (7) (Jun. 2012) 1–10, https://doi.org/10.1140/EPJB/E2012-30032-4, 2012 857.

[57] M.R. Ardigo, M. Ahmed, A. Besnard, Stoney formula: investigation of curvature measurements by optical profilometer, Adv. Mater. Res. 996 (2014) 361–366, https://doi.org/10.4028/WWW.SCIENTIFIC.NET/AMR.996.361.

[58] D.S. Rickerby, Internal stress and adherence of titanium nitride coatings, J. Vac. Sci. Technol. A Vacuum, Surfaces, Film. 4 (6) (Nov. 1986) 2809–2814, https://doi.org/10.1116/1.573683.

[59] Z.H. Cen, et al., Temperature effect on titanium nitride nanometer thin film in air, J. Phys. D Appl. Phys. 50 (7) (Jan. 2017), 075105, https://doi.org/10.1088/1361-6463/AA54E6.

[60] H. Tada, et al., Thermal expansion coefficient of polycrystalline silicon and silicon dioxide thin films at high temperatures, J. Appl. Phys. 87 (9) (Apr. 2000) 4189, https://doi.org/10.1063/1.373050.

[61] T. Middelmann, A. Walkov, G. Bartl, R. Schödel, Thermal expansion coefficient of single-crystal silicon from 7 K to 293 K, Phys. Rev. B Condens. Matter 92 (17) (Nov. 2015), 174113, https://doi.org/10.1103/PHYSREVB.92.174113/FIGURES/5/MEDIUM.

[62] G. Abadias, et al., Review Article: stress in thin films and coatings: current status, challenges, and prospects, J. Vac. Sci. Technol. A Vacuum, Surfaces, Film. 36 (2) (2018), 020801, https://doi.org/10.1116/1.5011790.

[63] E. Chason, B.W. Sheldon, L.B. Freund, J.A. Floro, S.J. Hearne, Origin of compressive residual stress in polycrystalline thin films, Phys. Rev. Lett. 88 (15) (Mar. 2002), 156103, https://doi.org/10.1103/PhysRevLett.88.156103.

[64] E. Chason, J.W. Shin, S.J. Hearne, L.B. Freund, Kinetic model for dependence of thin film stress on growth rate, temperature, and microstructure, J. Appl. Phys. 111 (8) (Apr. 2012), 083520, https://doi.org/10.1063/1.4704683.

[65] A. Saedi, M.J. Rost, Thermodynamics of deposition flux-dependent intrinsic film stress, Nat. Commun. 7 (1) (Feb. 2016) 1–6, https://doi.org/10.1038/ncomms10733, 2016 71.

[66] H. Windischmann, Intrinsic Stress in Sputter-Deposited Thin Films, 17, Jan. 2006, pp. 547–596, https://doi.org/10.1080/10408439208244586, 6.

[67] F.M. D'Heurle, J.M.E. Harper, Note on the origin of intrinsic stresses in films deposited via evaporation and sputtering, Thin Solid Films 171 (1) (Apr. 1989) 81–92, https://doi.org/10.1016/0040-6090(89)90035-7.

[68] I. Krylov, et al., Effect of the substrate on structure and properties of titanium nitride films grown by plasma enhanced atomic layer deposition, J. Vac. Sci. Technol., A 37 (2019), 60905, https://doi.org/10.1116/1.5109717.

[69] X. Chen, Y. Xi, J. Meng, X. Pang, H. Yang, Effects of substrate bias voltage on mechanical properties and tribological behaviors of RF sputtered multilayer TiN/CrAlN films, J. Alloys Compd. 665 (Apr. 2016) 210–217, https://doi.org/10.1016/j.jallcom.2015.10.076.

[70] B. Xia, J.J. Ganem, E. Briand, S. Steydli, H. Tancrez, I. Vickridge, The carbon and hydrogen contents in ALD-grown ZnO films define a narrow ALD temperature window, Vacuum 190 (Aug. 2021), 110289, https://doi.org/10.1016/J.VACUUM.2021.110289.

[71] C.E. Carlton, P.J. Ferreira, What is behind the inverse Hall–Petch effect in nanocrystalline materials? Acta Mater. 55 (11) (Jun. 2007) 3749–3756, https://doi.org/10.1016/J.ACTAMAT.2007.02.021.

[72] J.F. Archard, Contact and rubbing of flat surfaces, J. Appl. Phys. 24 (8) (Aug. 1953) 981–988, https://doi.org/10.1063/1.1721448.

[73] S.K. Bachani, C.J. Wang, B.S. Lou, L.C. Chang, J.W. Lee, Fabrication of TiZrNbTaFeN high-entropy alloys coatings by HiPIMS: effect of nitrogen flow rate on the microstructural development, mechanical and tribological performance, electrical properties and corrosion characteristics, J. Alloys Compd. 873 (Aug. 2021), 159605, https://doi.org/10.1016/J.JALLCOM.2021.159605.

[74] Z.N. Farhat, Y. Ding, D.O. Northwood, A.T. Alpas, Effect of grain size on friction and wear of nanocrystalline aluminum, Mater. Sci. Eng., A 206 (2) (Feb. 1996) 302–313, https://doi.org/10.1016/0921-5093(95)10016-4.

[75] Z.B. Qi, P. Sun, F.P. Zhu, Z.C. Wang, D.L. Peng, C.H. Wu, The inverse Hall–Petch effect in nanocrystalline ZrN coatings, Surf. Coating. Technol. 205 (12) (Mar. 2011) 3692–3697, https://doi.org/10.1016/J.SURFCOAT.2011.01.021.